
01 Jan 2023

A Study on the Impact of Silicon and Manganese on Peritectic Behavior in Low Alloy Steels Assisted by Mold Thermal Mapping Technology and Shell Growth Measurements

Damilola Balogun

Muhammad Roman

Rex E. Gerald

Missouri University of Science and Technology, geraldr@mst.edu

Laura Bartlett

Missouri University of Science and Technology, lnmkvf@mst.edu

et. al. For a complete list of authors, see https://scholarsmine.mst.edu/matsci_eng_facwork/2940

Follow this and additional works at: https://scholarsmine.mst.edu/matsci_eng_facwork



Part of the [Electrical and Computer Engineering Commons](#), and the [Metallurgy Commons](#)

Recommended Citation

D. Balogun et al., "A Study on the Impact of Silicon and Manganese on Peritectic Behavior in Low Alloy Steels Assisted by Mold Thermal Mapping Technology and Shell Growth Measurements," *Metallurgical and Materials Transactions B: Process Metallurgy and Materials Processing Science*, Springer, Jan 2023. The definitive version is available at <https://doi.org/10.1007/s11663-023-02764-x>

This Article - Journal is brought to you for free and open access by Scholars' Mine. It has been accepted for inclusion in Materials Science and Engineering Faculty Research & Creative Works by an authorized administrator of Scholars' Mine. This work is protected by U. S. Copyright Law. Unauthorized use including reproduction for redistribution requires the permission of the copyright holder. For more information, please contact scholarsmine@mst.edu.

A Study on the Impact of Silicon and Manganese on Peritectic Behavior in Low Alloy Steels Assisted by Mold Thermal Mapping Technology and Shell Growth Measurements



DAMILOLA BALOGUN, MUHAMMAD ROMAN, REX E. GERALD, II,
LAURA BARTLETT, JIE HUANG, and RONALD O'MALLEY

Non-uniform shell growth commonly caused by the peritectic transformation in low carbon and low alloy steels has been directly correlated with mold thermal maps using a mold immersion test into a molten steel alloy. Mold thermal maps were obtained by performing real-time temperature measurements with optical fibers embedded 1 mm from the mold working surface. Shell growth measurements were obtained by 3D optical scanning of the recovered steel shell following immersion testing. The effects of silicon and manganese on the shell growth and mold temperature maps have been examined in relation to the peritectic transformation for varying carbon contents. Results of thermodynamic and kinetic simulations using ThermoCalc and its kinetic module—DICTRA predicted that silicon expands the carbon content range to values between (0.12 pct C to 0.21 pct C) where peritectic behavior occurs and that manganese shrinks the carbon content range and shifts the range to lower carbon contents (0.06 pct C to 0.12 pct C). The results of these simulations were used to guide the selection of chemistries examined in the dip test experiments with the aim of validating the software predictions. Dip tests were performed at similar steel making temperatures that were used for the software simulations between 1600 °C and 1650 °C. Both software results and experimental observation showed relatively good agreement for the compositions examined.

<https://doi.org/10.1007/s11663-023-02764-x>
© The Author(s) 2023

I. INTRODUCTION

BREAKOUTS, surface quality problems and cracks must be avoided to produce high-quality steel.^[1–3] Understanding the effects of alloying elements on the as-cast quality of steel plays a very crucial role in this regard, particularly regarding their influence on peritectic behavior. Casting of steel compositions that fall within the peritectic sensitivity range is often avoided to avoid such quality and operating issues. Silicon and manganese are two elements that have opposing effects

on range of carbon contents that exhibit peritectic behavior during steel solidification: the former being a ferrite stabilizer while the latter stabilizes austenite. Ferrite stabilizers tend to narrow the austenite phase field by raising the eutectoid temperature while austenite stabilizers expand the austenite phase field by lowering the eutectoid temperature.^[4] Since the size of the austenite phase field and compositions of carbon at the peritectic transformation temperature are related as shown in Figure 1, silicon and manganese are known to produce different effects in carbon composition ranges at the peritectic transformation temperature. Even though the peritectic transformation should occur within a wider composition range such as C_A to C_C , experience has shown that it is the casting of steel grades between C_A and C_P that is most problematic for surface quality of as-cast slabs and formation of longitudinal cracks.^[2] Plain carbon steel grades containing carbon contents of between 0.1 and 0.18 pct, which are commonly referred to as depression prone grades, form primary delta-ferrite during solidification.^[5] This tendency to form delta-ferrite is usually measured in terms of the ferrite potential of the steel grade and it is related

DAMILOLA BALOGUN, LAURA BARTLETT, and RONALD O'MALLEY are with the Peaslee Steel Manufacturing Research Center (PSMRC), Department of Materials Science and Engineering, Missouri University of Science and Technology, Rolla, MO 65409. Contact e-mail: omalleyr@mst.edu MUHAMMAD ROMAN, REX E. GERALD II, and JIE HUANG are with the Department of Electrical and Computer Engineering, Missouri University of Science and Technology, Rolla, MO 65409.

Manuscript submitted September 29, 2022; accepted March 2, 2023.

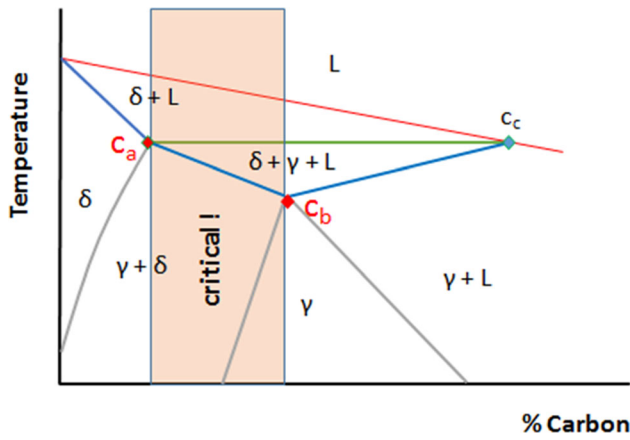


Fig. 1—Peritectic phase diagram showing relation between the boundaries of the peritectic sensitivity range and austenite phase field with (C_A to C_P) corresponding to the range of depression grades more prone to casting problems.

directly to the carbon content of the steel and the carbon equivalent of other elements in the steel, such as Mn and Si.^[5]

The ferrite potential and compositions of carbon equivalent for C_A and C_P are well-known for plain carbon steels and the nature of the peritectic transformation in such steels are already well-documented. For instance, the carbon content at the lower boundary of the peritectic— C_A and peritectic point— C_P have already been thermodynamically determined to be around 0.1 and 0.18 pct, respectively, for plain carbon steels. Within this range, the steels have the greatest tendencies for defect formation, such as surface longitudinal cracks and many forms of non-uniform shell growth such as shell buckling, wrinkling and deformation, which occur because of shell shrinkage resulting from the volumetric contraction that accompanies the δ/γ transformation during the initial solidification stages. The shell deformation creates roughness of the shell leading to formation of localized airgaps that reduce the mold heat transfer between solidifying shell and copper mold, which often causes surface cracks in the shell.^[6–8]

Xu *et al.*,^[9] have studied the effects of elements on the peritectic reaction in molten steel using thermodynamic analysis. FactSage software was used in their study to calculate C_P by creating phase diagrams and determining the relationship between the alloying elements – manganese, silicon, aluminum, phosphorus, and sulfur on the C_P value using multivariate nonlinear regression. They found no effect of silicon on C_P in the range of 0 to 0.5 mass pct. In the presence of other alloying elements however, silicon had an effect on the C_P value because of the interaction between silicon and other alloying elements. Manganese was found to affect the peritectic point to a larger degree and causes the peritectic point to move to the left. The investigators found that an increase in manganese content from 0 to 1.5 mass pct causes a decrease in C_P from 0.172 to 0.138 pct C. The investigators concluded that manganese has a large effect on the C_P . In a similar fashion, Sarkar *et al.*,^[7] reported that manganese, being an austenite stabilizer,

shifts all the peritectic compositions including C_A , C_P , and C_C to the left while silicon simply has the opposite effect. Their report relied on the creation of many pseudo binary Fe–C phase diagrams using ThermoCalc version S and the TCFE7 database to determine the influence of each alloying element on the relevant peritectic compositions.

Furthermore, the desire to manufacture vehicles with reduced weight is currently leading the automobile industry to rely on steels with peritectic composition. Some of the steels that are within the peritectic composition range are advanced high strength steels (AHSS) and high strength low alloy steel (HSLA). These steels are also used in other products due to their excellent mechanical properties.^[10–12] Aside from the automobile industry, peritectic steels are also used in manufacturing pipelines, naval vessels and bridges.^[13,14] There is therefore the need to produce steels with no defects.^[10,15]

In a recent mold simulator study of the heat transfer during initial solidification in a continuous casting mold, Zhang and Wang developed a one-dimensional inverse heat transfer problem for solidification (1DITPS) and a two-dimensional inverse heat conduction problem (2DIHCP).^[11] The 1DITPS was used to determine the temperature distribution and heat transfer through a solidifying steel shell using the measured shell thickness, while the 2DIHCP was used to estimate the copper mold wall temperature distribution from the measurements obtained by sub-surface temperature sensors. Coupled with measurements of liquid slag thickness, the 1DITPS and the 2DIHCP were used to determine mold/slag interfacial thermal resistance, liquid film thermal resistance, mold/shell interfacial thermal resistance and solid film thermal resistance. For the experiments in their work, a mold simulator equipped with a mechanism for shell extraction was designed and used. Shell extraction permitted the withdrawal of the solidifying shell, hence mimicking a strand casting process. With their results, it was also possible to determine the percentage of solid film thermal resistance over the total mold/shell thermal resistance. Similarly, a mold simulator was used by Zhang *et al.*,^[12] to reproduce the continuous casting process on a laboratory scale. In their work, a novel simulator was used to simulate the solidification of a continuously cast slab. Surface heat flux and solidification structure was compared for both a physical simulation sample and an actual continuously cast slab. It was reported that the physical simulation sample gave a good representation of the continuously cast sample in terms of its ability to reproduce both heat transfer and solidification process.

The inverse heat conduction problem was also used to calculate the interfacial heat transfer during sub-rapid solidification of a medium manganese steel by calculating the temperature gradient inside the cooling mold. In this work, a droplet solidification technique was used with the purpose of revealing the effect of naturally deposited film on the heat flux, wettability, and as-cast structure. Lu *et al.*, reported that the wettability of a water-cooled copper mold/steel droplet system improves after deposition since the contact angle between the

couple became lower (from 111.539 to 82.217 deg) with subsequent dropping test.^[13] It was also reported that the time from the start of ejection to the initiation of solidification decreased from 1.76 to 1.28 seconds during the tests meaning the steel remained in the liquid phase longer, thus leading to an increase in the heat flux with deposition of the natural film. This leads to an overall reduction in the interfacial thermal resistance. The last two attempts have successfully demonstrated the use of both 1DITPS and 2DIHCP for the computation of surface heat flux from temperatures obtained from embedded temperature sensors. The temperature sensors that were used in those studies were capable of point-by-point data accumulation which means that the resolution of temperature measurements is limited. Moreover, the inverse heat conduction problem is subject to many computational errors which have still not yet been fully accounted for.

While the drawbacks of the peritectic transformation are well-known for plain carbon steels, the role of higher levels of alloying elements have not been well-documented. Most earlier studies on this subject rely predominantly on the creation of many thermodynamic phase diagrams from which the deviation of the peritectic compositions as a function of alloying element was determined. While thermodynamics is a great tool for the prediction of phase and phase stability, it offers no way of observing and determining the extent to which the peritectic transformation has occurred from the standpoint of observable physical features. Two of such physical features are the shell thickness variations and the mold temperature history which can be presented as a mold thermal map. The present paper seeks to identify the compositional shift in the relevant peritectic compositions as a function of silicon and then as a function of manganese using physically identifiable features on both steel shell and copper mold thermal map. This task was accomplished in two major steps. In the first step, the compositional shift as a function of silicon and manganese were estimated independently using ThermoCalc 2019a and its kinetic-based module DICTRA. The range of silicon and manganese studied in this work were, respectively (0.05 to 2.5 pct) and (0.05 to 3.5 pct) which are composition ranges found in commercial steels. The element databases for both ThermoCalc and DICTRA simulations were TCFE: Steels/Fe-Alloys v9.0 and MOBFE4: Steels/Fe-Alloys Mobility v4.0, respectively. Simulation temperatures were chosen to match normal steel making temperatures around 1600 °C and a planar geometry was chosen for the physical domain used in the DICTRA simulations. In the second stage, experiments immersion tests were performed in a 200 lbs. induction furnace using steel chemistries like the ones used in the thermodynamic simulations with the purpose of determining the alloy effect on the peritectic compositional shift using physically identifiable features like shell growth anomaly and mold thermal maps. Carbon was varied between successive dips between 0.11 pct C and 0.19 pct C for the silicon-based experiments and between 0.02 pct C and 0.13 pct C in the manganese-based experiments. These ranges were

chosen in an attempt to capture both peritectic and non-peritectic composition ranges. High-resolution distributed fiber-optic sensors, based on Rayleigh OFDR (optical frequency-domain reflectometry) technology, were used to generate mold thermal maps.^[16] In the present work, these mold thermal maps have been directly correlated with shell growth measurement maps in a manner that has not been reported previously in literature.

II. EXPERIMENTAL PROCEDURES

A. Simulation with ThermoCalc Diffusion Module: DICTRA

In processes that are diffusion-controlled, DICTRA makes it possible to perform diffusion simulations with conditions that are realistic in the solidification and processing of practical alloys. The peritectic reaction has been found to be a diffusion-controlled process driven by solute redistribution and liquid supersaturation.^[17,18] Based on numerical solution of the multi-component diffusion equations, a prediction of the compositional shift effect of Si and Mn were performed individually in DICTRA 2019a software package. The element databases used for these calculations are TCFE9: Steels/Fe-Alloys v9.0 and the mobility databases—MOBFE4: Steels/Fe-Alloys Mobility v4.0. All calculations were set-up using a 1-D linear model as shown in Figure 2. To represent the smallest unit length of microsegregation from the center of the dendrite to the center of the interdendritic region, only one half of the SDAS was required for calculations. This is because the solidification can be assumed to proceed symmetrically at the secondary dendrite scale.

The compositions studied for these simulations were limited to Fe–C–Mn–Al–Si. This simplification was necessary in order to closely match the steel compositions to be made for dip testing and also to reduce the overall run time for the model. Figure 3 presents a summary of the steps involved in the simulation. This simulation which handles moving phase boundaries assumes that local equilibrium exists at the phase boundaries and that the formation of new phases—FCC and BCC become stable.

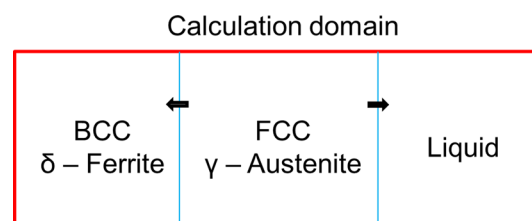


Fig. 2—Schematic of the cell set-up showing the three phases of interest to the simulation and their interfaces. The arrows indicate the direction of growth of the austenite phase which should eventually consume both the liquid and ferrite phases.

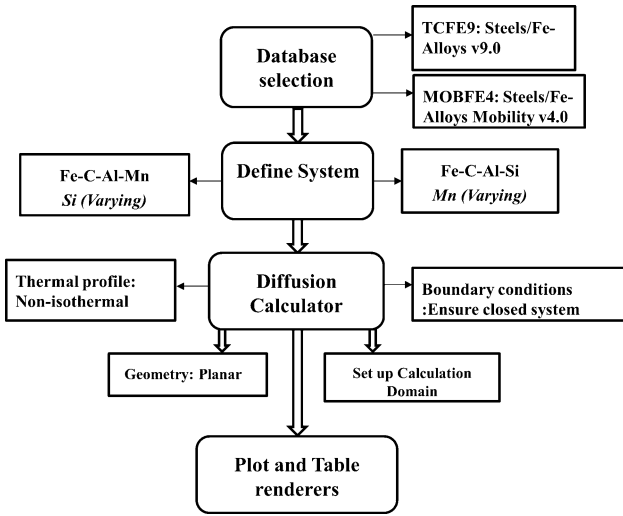


Fig. 3—Step by step process involved in the DICTRA simulation showing the two separate stages in which calculations were performed—varying silicon and then varying manganese to determine their effects on C_A , C_P and C_C .

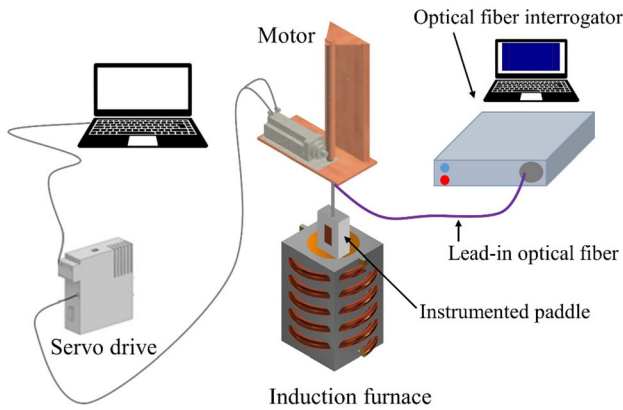


Fig. 4—Schematic of the dip test experiment set-up including the optical fiber interrogation system based on optical frequency-domain reflectometry.

The chemical potentials of all the elements on either side of the phase boundaries were used as a driving force for the flux calculations. In order to maintain simulation stability, the maximum allowed time step was set as 10 pct of the total simulation time and the simulation time was determined by the cooling rates which was applied. For both sets of simulations, a high cooling rate of 65 °C/s was assumed and the SDAS was calculated using the empirical relation in Eq. [1], reported by Earl-Bealey and Thomas. The SDAS was then used to determine the width of the calculation domain.^[19]

$$\lambda_{SDAS}(\mu m) = (169.1 - 720.9 \times C_C) \times C_R^{-0.4935} \text{ for } 0 < C_C \leq 0.15 \quad [1]$$

where C_C is the carbon content (wt pct C) and C_R is the cooling rate (°C/s).

Table I. Composition Matrix for Investigating the Effect of Silicon on the Peritectic Compositional Shift

Carbon (Constant)	Manganese (Constant)	Aluminum (Constant)	Silicon (Varying)	Fe (Balance)
0.13	0.05	0.05	0.05	Bal
0.12	0.05	0.06	0.5	Bal
0.11	0.05	0.05	1.5	Bal
0.12	0.05	0.05	2.0	Bal
0.13	0.05	0.06	2.6	Bal

As stated earlier, two sets of calculations were performed with this model. The first set of simulations investigated the compositional shift effect of silicon on the relevant peritectic compositions— C_A , C_P , and C_C , while the second set explored the effect of manganese on the peritectic composition.

A schematic of the apparatus is presented in Figure 4. The copper mold (100 mm × 50 mm × 12 mm thick) was instrumented with optical fibers (o.d. = 250 μm), which were embedded in fine slots that were cut to 1 mm from the hot surface of the mold that was exposed to molten steel. Details of test paddle and instrumentation of copper block with optical fibers have been well-documented in previous work.^[16,20]

III. RESULTS AND DISCUSSION

A. Effect of Silicon: Simulation

The effect of silicon on the carbon compositional shift at the peritectic was investigated by running ThermoCalc equilibrium and DICTRA simulations for various steel chemistries which contained varying levels of silicon but the same level of manganese and other elements. In other words, while the remaining alloying elements were kept low and constant, silicon was varied according to Table I. The compositions of interest are the carbon concentrations at the liquid/ferrite interface C_A and the carbon concentration at the peritectic point C_P at the peritectic transformation temperature. For the case of the ThermoCalc equilibrium portion of the calculation, these values were easily obtained from the resulting phase diagram.

For the DICTRA portion of the calculation, C_A and C_P were obtained directly from the respective interfaces on a plot of time and composition of interface as shown for one of the instances in Figure 5. The plot shows how the carbon concentration at the liquid/ferrite interface change in the primary solid phase—ferrite during solidification with time.

Initially there was an increase in carbon concentration with time indicating a buildup of solute at the ferrite/liquid interface up to a maximum value which is the C_A value signifying the maximum amount of carbon that can be dissolved in the δ -ferrite phase which also corresponds to the carbon concentration at the tip of the nose in the δ -ferrite phase of the phase diagram.

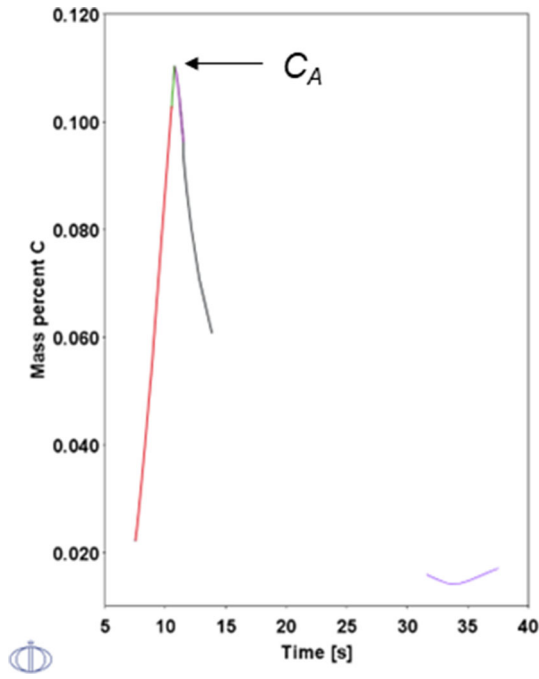


Fig. 5—Change in carbon composition with time in the ferrite phase for determining the lower boundary carbon concentrations as the maximum carbon dissolved in the ferrite phase— C_A .

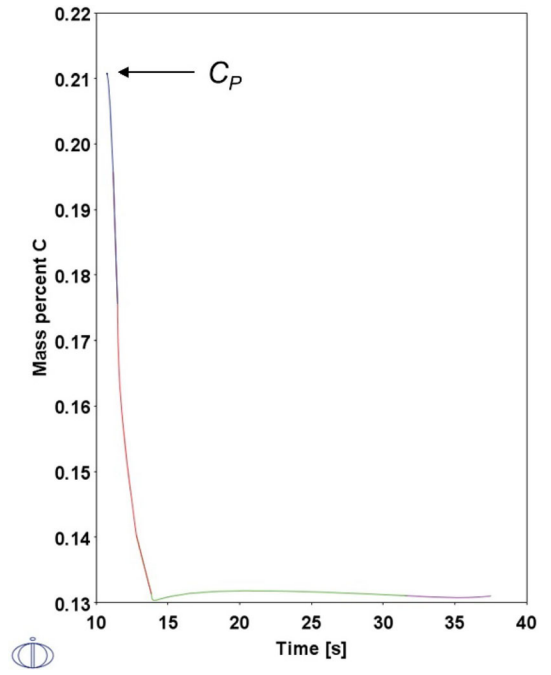


Fig. 6—Time-dependent interface composition for the austenite phase shows upper boundary of the peritectic carbon concentration to be 0.21-C.

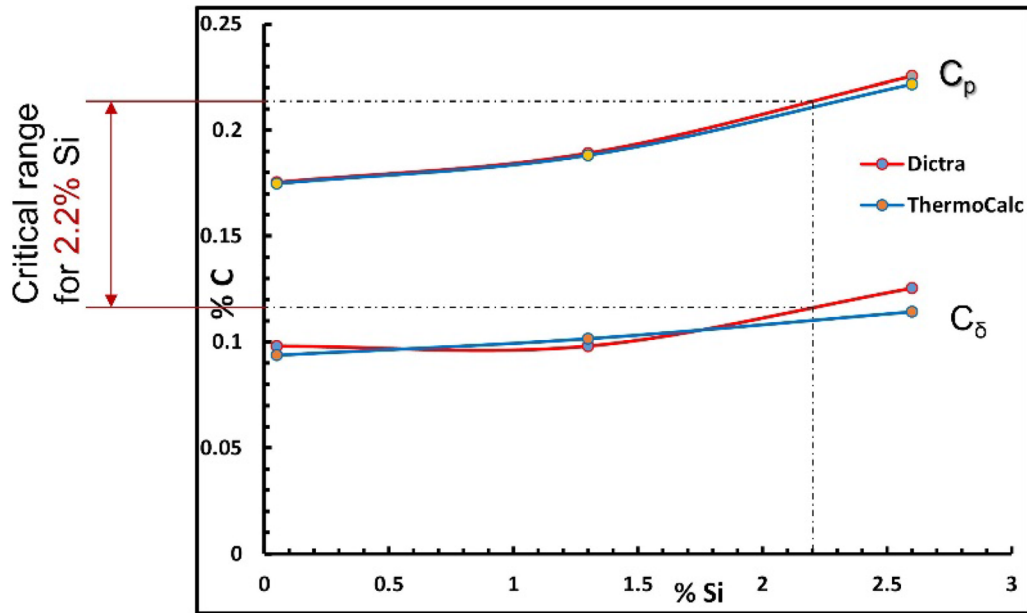


Fig. 7—Effect of silicon on the peritectic boundary concentrations using thermodynamic and kinetic simulations show that silicon expands the compositional carbon range and shifts the peritectic to higher carbon concentrations.

The determination of the upper boundary carbon concentration, *i.e.*, C_P followed a similar approach. However, the composition of interest to the present study is the carbon concentration at the triple point where the three phases—liquid, ferrite and austenite coexist. Coincidentally, the first crystals of austenite that precipitate from the peritectic reaction will have the

same carbon concentrations as the triple point. This concentration is obtained on a plot of the interphase concentrations with time as shown in Figure 6.

Having obtained the carbon concentrations at the lower and upper boundaries of the peritectic, similar calculations were performed for higher concentrations of silicon to determine the lower and upper boundary

Table II. Steel Chemistries for Dip Test Experiments

Test Level	Carbon		Silicon		Manganese		Aluminum	
	Aim	Measured	Aim	Measured	Aim	Measured	Aim	Measured
1	< 0.11	0.06	2.2	2.2	0.06	0.06	0.06	0.03
2	0.11 to 0.22	0.11	2.2	2.1	0.06	0.05	0.06	0.02
3	0.11 to 0.22	0.14	2.2	2.1	0.06	0.05	0.06	0.01
4	> 0.25	0.19	2.2	2.0	0.06	0.05	0.06	0.008

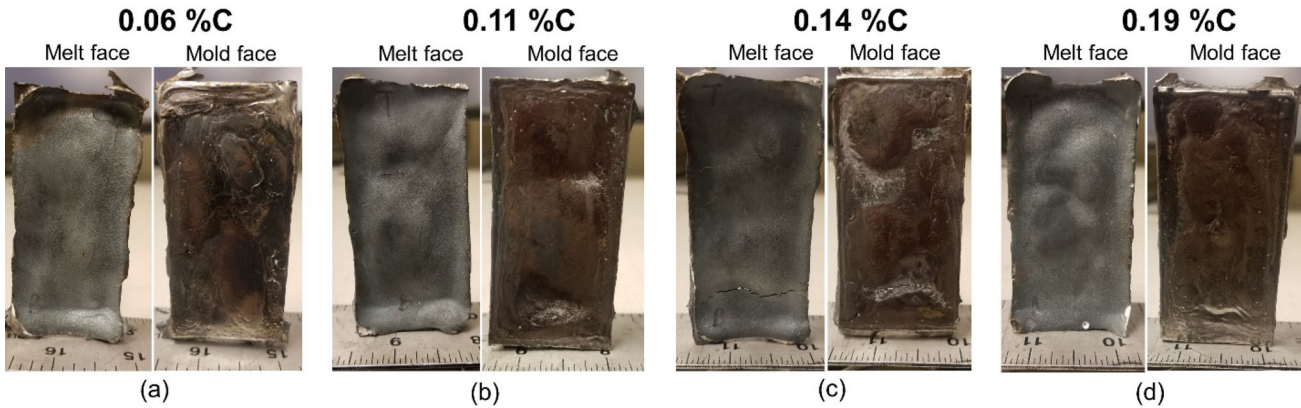


Fig. 8—Photos of 2 pct wt Si steel shells cast with (a) 0.06 pct C (b) 0.11 pct C (c) 0.14 pct C and (d) 0.19 pct C showing both melt and mold faces of each shell.

carbon concentrations. Figure 7 clearly depicts the compositional shift resulting from silicon addition. At 2.2 pct wt silicon, the peritectic range has now become (0.12 pct C to 0.21 pct C), indicating that the addition of silicon has shifted the peritectic compositions to higher carbon ranges. The knowledge of these predictions was useful for designing a dip test experiment that involved immersing a fiber-optic instrumented copper chill into a molten steel bath.

1. Dip test evaluations

The peritectic transformation in steels is known to impact initial shell formation. The first layer of steel that solidifies against the copper mold can experience various forms of shell growth non-uniformities, such as thickness variation, buckling and depressions. The purpose of the dip test experiments performed in the present work was to produce steel shells whose compositions span composition ranges that are in both peritectic and non-peritectic ranges as predicted by the kinetic and thermodynamic model previously obtained. The tests were conducted with a computer-controlled dip tester which used a servo drive and motor to control motion parameters. Twelve slots were machined in the copper mold plate to accommodate optical fiber. The slots were instrumented with a single continuous optical fiber

configured with multiple return loops at both ends of the mold plate. Temperature measurements were based on acquiring and interpreting Rayleigh backscattering signals from the fiber under test. A fiber-optic interrogator, based on optical frequency-domain reflectometry (OFDR), was used to acquire and process Rayleigh scattering signals. The spatially distributed temperatures along the length of the optical fiber were metered with a 0.65-mm spatial resolution. The measurements were recorded with an update rate of 25 Hz. The spatially distributed temperature measurements were used to generate 2D thermal maps of the mold surface during immersion of the mold into the molten metal and subsequent solidification of the metal shell against the mold surface. More details on the mold instrumentation and thermal maps were provided in a previous publication.^[16]

In this experiment, four immersion tests were performed in succession. Between each immersion, a predetermined amount of graphite was added to the bath to increase the carbon concentration of the molten steel progressively, thereby capturing both peritectic and non-peritectic carbon concentrations. As shown in Table II, the tests were performed for a 2 pct Si steel and the carbon range tested was selected to closely match the DICTRA software model predictions.

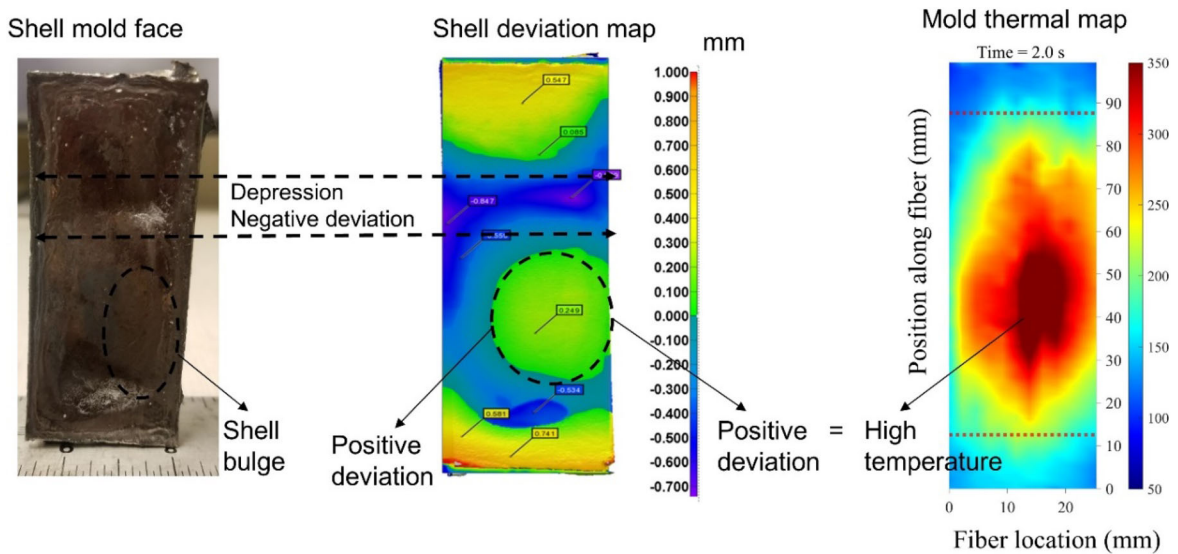


Fig. 9—Photo of 0.11 pct C shell with shell deviation map and instantaneous snapshot of mold thermal map at 2.0 s after immersion. The area between the red dotted lines on the mold thermal map is the area of the copper mold exposed to the molten steel.

As can be seen from the table, the aim of the dip tests was to test within and outside of the peritectic boundaries. However, the aim carbon level was not achieved at the upper boundary in this experiment, *i.e.*, while a 0.25 pct carbon concentration was targeted, the actual carbon concentration measured was 0.19 pct in the final dip test, which was still predicted to be within the peritectic range in the simulation results. As will be seen later, the mold thermal maps show a much slower mold heating rates for these peritectic compositions compared to the non-peritectic compositions. During immersion, which lasted for a duration of 4 seconds for each carbon level, a steel shell was formed against the copper block in each test as shown in Figure 8. The photos suggest that the non-peritectic shells in Figures 8(a) and (b) solidified evenly as seen in their smooth appearance. Shells in Figures 8(c), and (d) within the peritectic composition range however showed greater degree of unevenness. Real-time mold temperatures were recorded by the embedded optical fibers and these temperatures were used to generate mold thermal maps. The four solidified shells were recovered from the molds easily at room temperature and scanned in three dimensions (3D).^[21]

3D Scanning was achieved using a metrology-grade blue light scanner (OptimScan™—5 M from Shining 3D) which reconstructs the exact 3D model of the shells. See Appendix—Figure A1. Using dedicated software, the shell 3D models were post processed to obtain relevant information such as the degree of shell deviation from normal flatness and the shell thickness variations. A detailed description of steps involved in obtaining the shell deviation and shell thickness variation has been previously reported.^[20,22] Shell deviation which is any

departure of the shell surface from complete flatness can predict shell pull away during continuous casting of steel. This ultimately affects the contact area between solidifying shell and copper mold. To obtain this deviation, the shell model was aligned with a computer aided design (CAD) model having similar dimensions with the shell. In this process, the CAD model is the reference model while the shell model is the object whose deviation is to be measured. The shell's deviation from the reference model is measured and then represented as a color map super imposed on the reference model. Combined with the scale markers, a quick survey can reveal areas of the shell that are positively deviated (elevated above the reference model) and negatively deviated (below the reference model). Hence the imperfect contact which the solidifying shell made with the copper mold can be represented as color maps. The shell, shell deviation maps, and snapshots of the corresponding mold thermal maps are pictured in Figure 9 for a non-peritectic (0.11 pct C) and Figure 10 for a peritectic (0.19 pct C). It was observed that areas on the shell deviation map with positive deviation suggested that there was good thermal contact between solidifying shell and the copper mold as those correspond to areas that registered higher temperatures in the mold thermal maps.

Instantaneous snapshots of the real-time thermal maps of the four molds are presented in Figure 11 at times corresponding to 0.5, 1, 1.5, and 2 seconds after immersion. Mold thermal maps were obtained using spatially distributed temperature profiles along embedded optical fiber sections during the immersion tests. See Appendix—Figure A3.

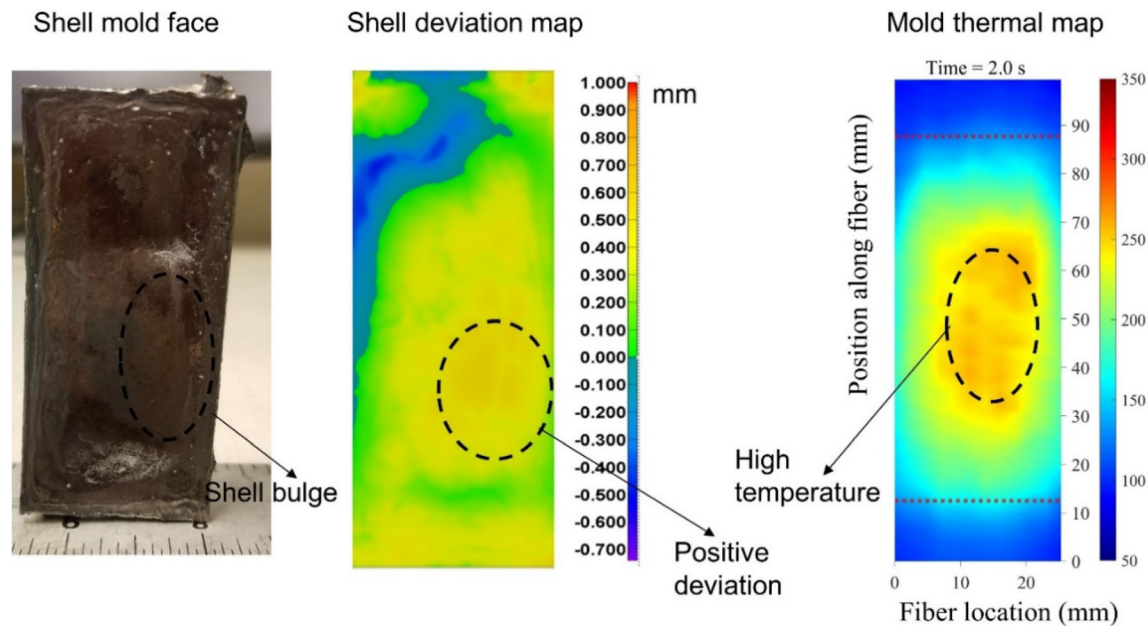


Fig. 10—Photo of 0.19 pct C shell with shell deviation map and instantaneous snapshot of mold thermal map at 2.0 s after immersion.

It was observed that in the steels whose carbon concentration were in the peritectic range as predicted by the DICTRA simulation results, the mold thermal maps clearly indicated significantly lower heating rates. This suggests that a lower heat conductivity medium (air gap) must have been present between the solidifying shell and copper mold which contributed to the reduction in transfer of heat from the solidifying shell and the mold. Similar experiments were conducted separately to investigate the effects of a high manganese concentration on the peritectic behavior of a plain carbon steel as discussed subsequently.

To further investigate the possible effects of the peritectic solidification on the heating rate and shell deviation, instantaneous temperature profiles for a peritectic and a non-peritectic chemistry have been provided in Figure 12. The temperatures were obtained from the optical fiber strand placed at the middle of the mold—embedded 1 mm from the hot surface. Here, it may be observed that similar locations that registered higher temperatures in the mold that was immersed in the non-peritectic steel, recorded lower temperatures in the peritectic steel—an indication of the lower heat removal rate in the peritectic.

More work was also done to characterize the nature of the peritectic transformation by comparing shell deviation for a peritectic and a non-peritectic steel chemistry. This is a quantitative method to investigate the degree of shell unevenness. Like the temperature profiles, shell deviation was compared longitudinally down the middle of the shells and this comparison is shown in Figure 13.

The shell deviation profiles for the two chemistries show contrasting trends whose nature is still been investigated. It is however clear that the magnitude of shell deviation observed in peritectic shells is greater than those observed in non-peritectic shells as shown in Figure 14.

B. Effect of Manganese—Simulation and Dip Test Evaluation

The setup and procedures involved for both simulation and experimental assessment, respectively, have been previously discussed in the preceding sections. To determine the compositional shift in carbon concentration because of manganese additions, DICTRA calculations were again performed for varying amounts of manganese precisely starting from no manganese up to about 4.0 pct wt Mn. In each of the manganese levels the lower and upper boundary peritectic carbon concentrations were determined in a similar manner as described. Figure 15 shows that manganese additions have a significant effect on the peritectic compositions by shifting the carbon concentrations to low values for both lower and upper boundaries hence, shrinking the peritectic gap. For example, a manganese addition causes a shift in the peritectic gap from (0.09 to 0.17) pct wt at no manganese to (0.06 to 0.12) pct wt at 2.0 pct wt Mn.

Dip tests experiments were designed with compositions like those obtained from the simulation results in a manner like the experiments conducted with silicon. In this case a 2 pct wt Mn steel was investigated, and the

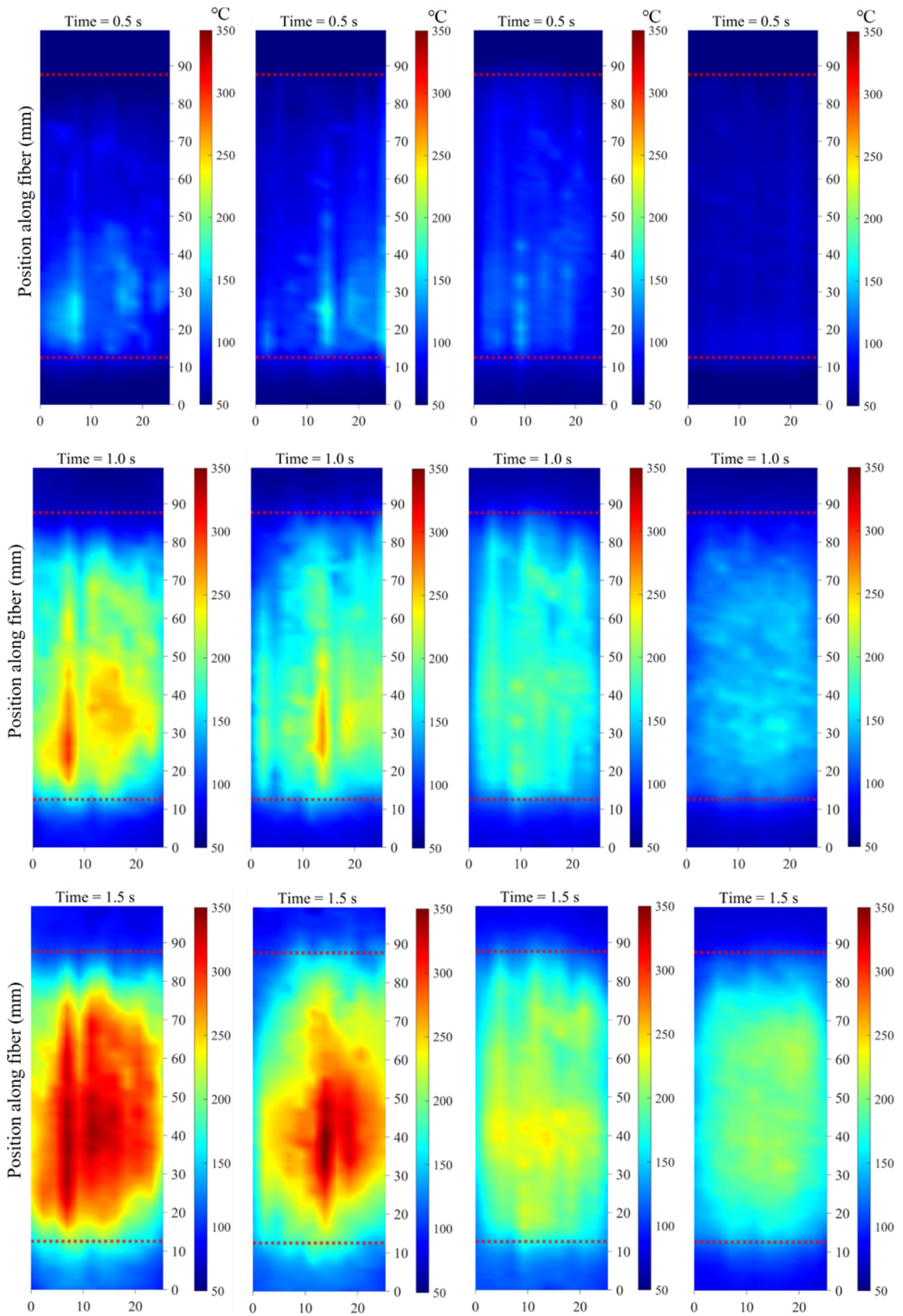


Fig. 11—Snapshots of the 4 mold thermal maps at 0.5, 1, 1.5, and 2.0 s of immersion shows slower heating rates in the molds of peritectic composition immersed.

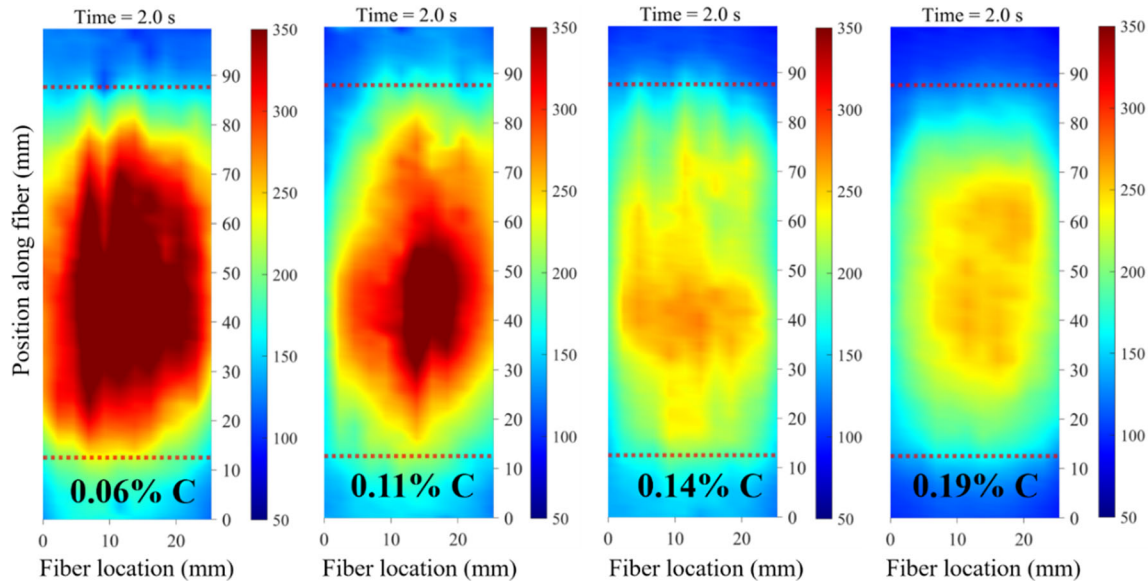


Fig. 11—continued.

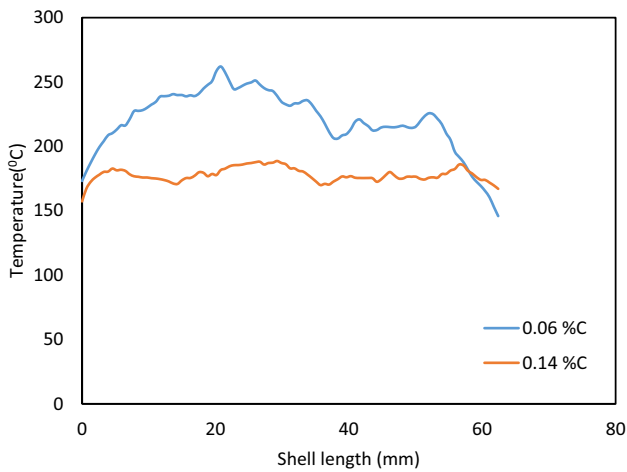


Fig. 12—Temperature profiles for peritectic and non-peritectic at mold center.

carbon concentrations were varied from 0.02 to 0.16 pct wt C in a manner that allowed testing to be carried through that predicted peritectic range for a 2 pct wt Mn steel. The steel chemistries used in the present dip tests are presented in Table III.

Once again, four immersion tests were performed in succession and carbon levels were varied between each test by adding a predetermined amount of graphite into the molten bath. As can be observed in Table III, it was required to add predetermined amount of aluminum into the bath in order to maintain the aluminum content within acceptable range. This addition was done after the second dip. A picture of the dip testing apparatus

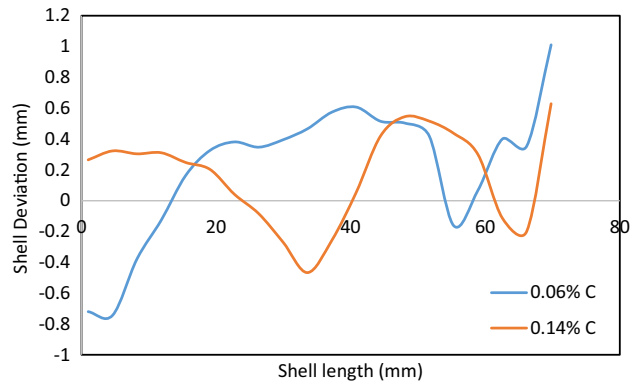


Fig. 13—Shell deviation profile at center of peritectic shell (0.14 pct C) and non-peritectic shell (0.06 pct C).

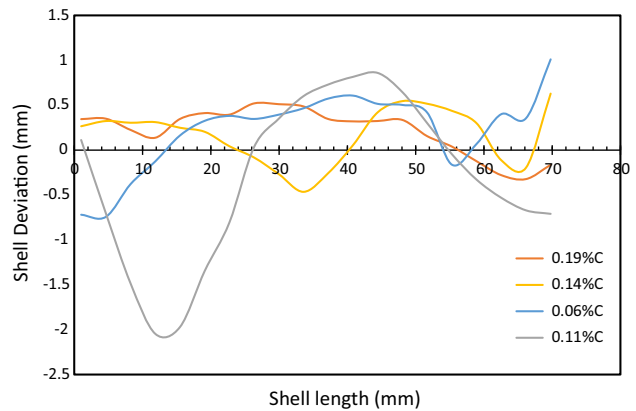


Fig. 14—Shell deviation at the center of the four shells show greater deviation in the peritectic shells.

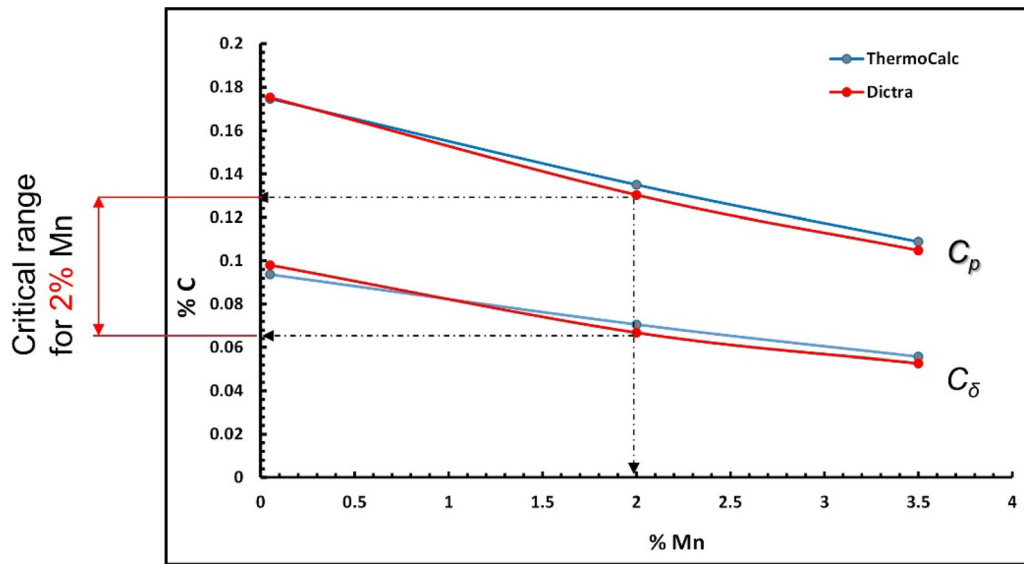


Fig. 15—Effect of manganese on the peritectic boundary concentrations using thermodynamic and kinetic simulations show that manganese shrinks the compositional carbon range and shifts the peritectic to lower carbon concentrations.

Table III. Steel Chemistries from Dip Test Analyzed with Optical Emission Spectroscopy and LECO (C/S)

Element	Dip1	Dip2	Dip3	Dip4
Aluminum (Wt Pct)	0.06	0.05	0.05	0.04
Manganese (Wt Pct)	2.1	2.0	2.0	2.0
Silicon (Wt Pct)	0.06	0.07	0.06	0.06
Carbon (Wt Pct)	0.02	0.04	0.06	0.13

taken during one of such immersion tests is shown in Figure 16. During the melting stage of the experiments, care was taken to minimize prolonged and unnecessary exposure of the molten bath to atmosphere. Melting was also done under argon inert atmosphere. After cooling to room temperature, the four shells were recovered, and post processed using 3D scanning in the same way as previously described.

The shells recovered after the dip tests are pictured in Figure 17. Since the surface quality of a continuously cast steel product is largely determined by the early stages of solidification in the mold,^[21] a quick visual examination revealed that the thickness variation and non-uniform growth was more pronounced in the steel shells cast at 0.04 and 0.06 pct C with the latter in the peritectic range as predicted by the DICTRA simulation. The surface deformities were caused by irregular growth of the shell at the vicinity where the solidifying shell first contacted the copper mold. As the temperature of the steel dropped rapidly below the peritectic point, a new solid phase—*austenite* forms by reaction between

the initial ferrite phase and pre-existing liquid phase by a peritectic reaction. As the *austenite* solid phase is denser than the initial primary ferrite, this transformation results in a volumetric shrinkage that causes non-uniformity in the shell growth.^[23,24] It is therefore obvious that the manganese addition has shifted the peritectic compositions where non-uniform shell growth occurs to lower carbon contents in contrast to silicon which was shown previously to shift the peritectic composition to higher carbon concentrations.

The shells were again scanned in 3D to obtain three dimensional models which were processed to determine the shell thickness non-uniformity and thus obtain thickness color maps. Once again, real-time mold thermal maps were created from the optical fiber temperature measurements. The mold thermal maps were found to correlate well with the shell thickness maps. Specifically, it was observed that areas of the shell with high thickness were the same areas where higher temperatures were recorded. Conversely, thinner spots on the shell were correlated with parts of the mold that recorded lower temperatures. These comparisons are shown in Figure 18. The observations are explained by the fact that shell growth is directly related to the rate of heat extraction by the copper mold from the molten steel through the solidifying shell. Hence, higher heat removal will correspond to higher temperature recorded and a thicker shell where contact between the mold and steel shell is good. Center-line shell thickness profiles also revealed rapid fluctuations in the peritectic grades. See Appendix—Figure A2.

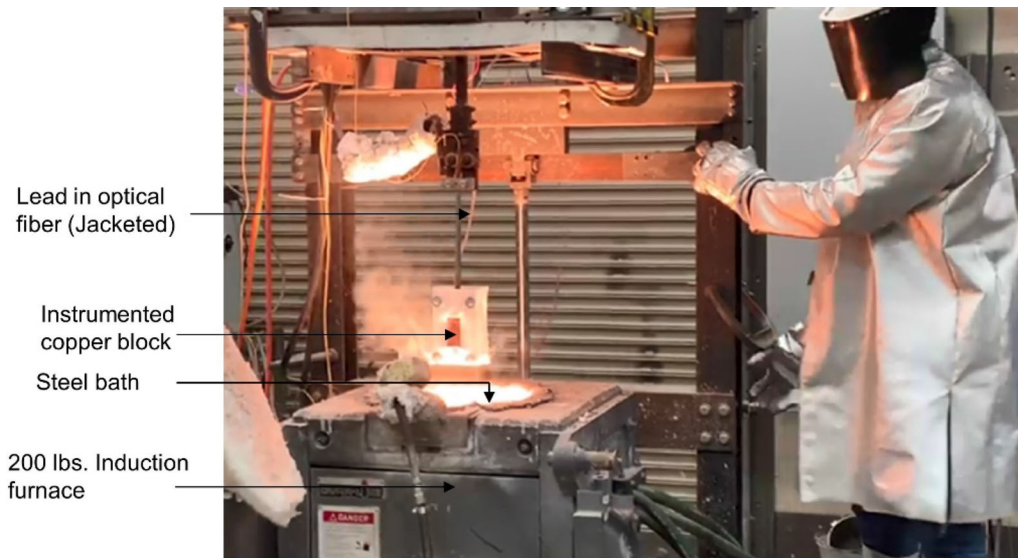


Fig. 16—Dip test experiment showing progress of immersion of test paddle comprising fiber-optic instrumented copper block (encased) into molten steel bath contained in a 200 lbs. induction furnace.

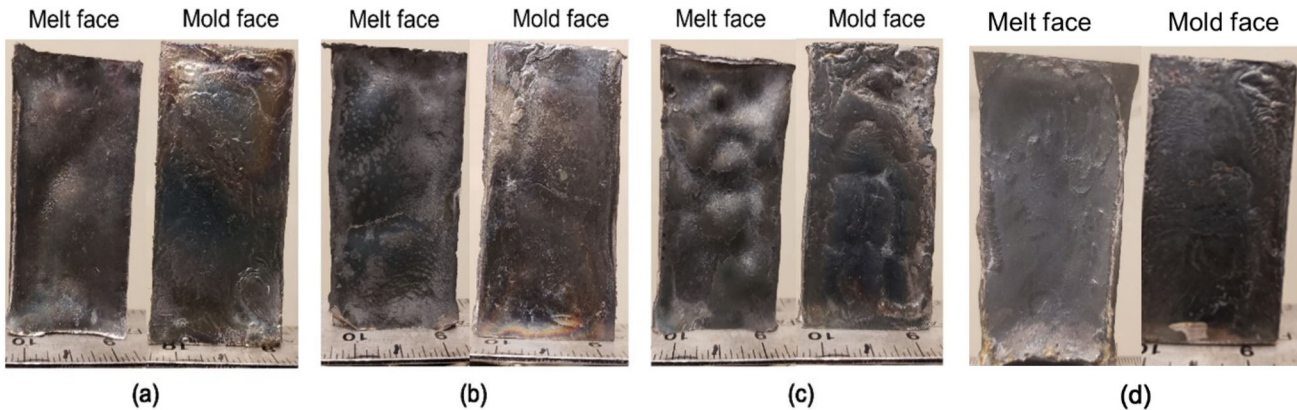


Fig. 17—Photos of 2 pct wt Mn steel shells cast with (a) 0.02 pct C, (b) 0.04 pct C, (c) 0.06 pct C, and (d) 0.13 pct C showing both melt and mold faces of each shell.

Earlier, it was found that the peritectic composition range in the presence of 2 pct Mn should be in a carbon range from 0.06 pct C to 0.128 pct C. However, as observed from the mold thermal map and steel shell cast at 0.04 pct C, non-uniform shell growth was observed at this composition, which is below the composition predicted by software modelling for where the peritectic behavior should be expected. An interesting area of further study would involve performing similar dip tests for different manganese compositions, varying carbon concentrations in each of those immersions in a similar manner conducted in the present work to explore the boundaries of this behavior. Such a trend could then be compared with the thermodynamic and kinetic simulations earlier presented previously to improve our ability to predict the range of peritectic sensitivities for these steels.

IV. CONCLUSION

Manganese and silicon have opposing effects on the carbon concentration range where peritectic behavior and shell growth non-uniformity occurs in plain carbon steels containing high levels of Mn and Si. It was observed that while silicon tends to expand the peritectic sensitivity window, manganese shrinks the range and moves the concentrations to lower carbon levels. The impacts of silicon and manganese are related to the individual effects of both elements on the ferrite and austenite phase fields, respectively. Therefore, higher manganese concentrations stabilize the austenite phase and enhances the peritectic transformation. The secondary solid phase—austenite which forms crystallizes as a face centered cubic (FCC) structure which is denser than the primary solid phase—delta-ferrite which is a body centered cubic (BCC) crystal. This change in

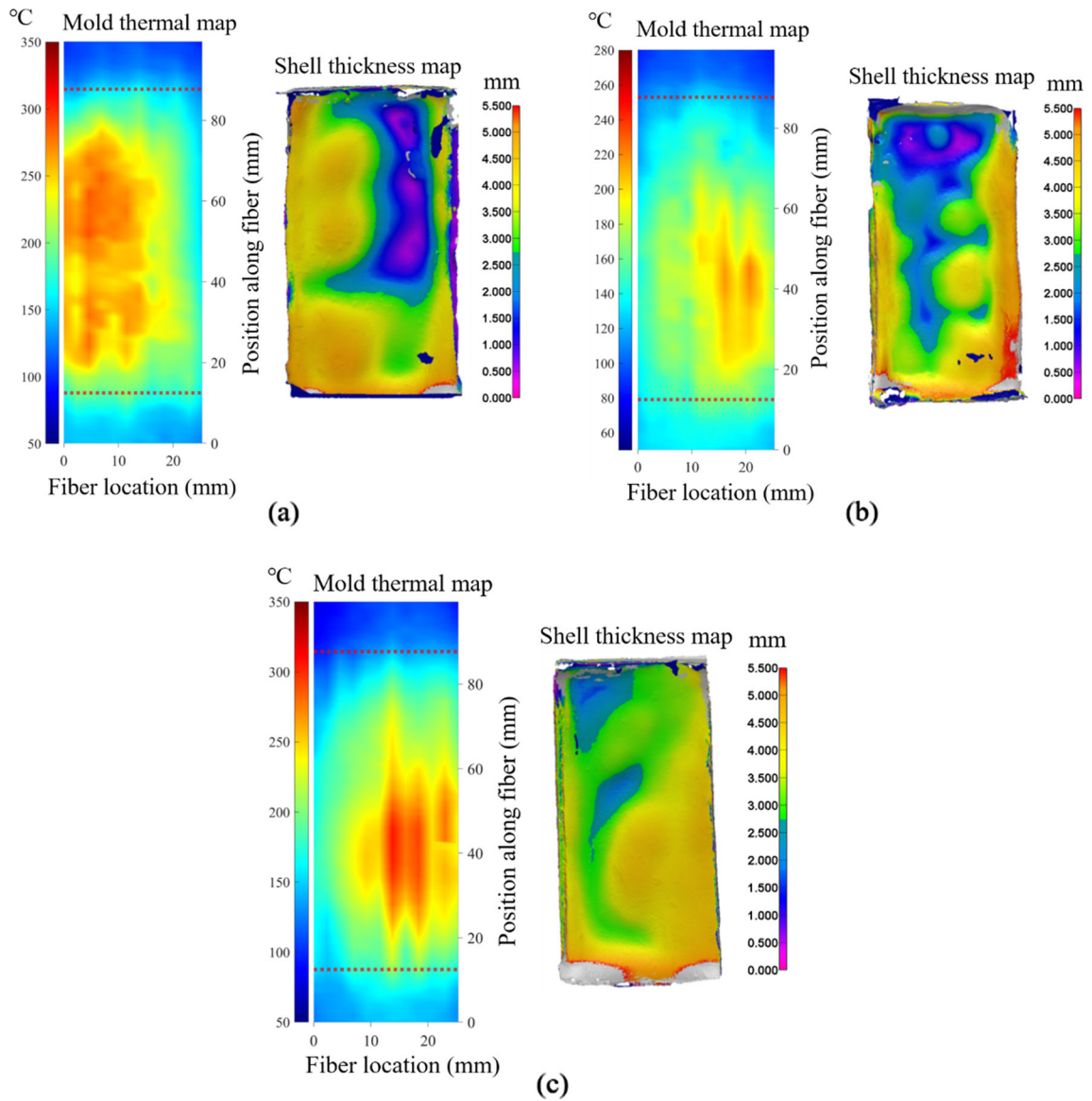


Fig. 18—Snap shots of mold thermal maps and corresponding shell thickness maps (a) mold thermal map and shell thickness maps for 0.02 pct C shell (b) mold thermal map and shell thickness map for 0.06 pct C shell (c) mold thermal map and shell thickness map for 0.13 pct C shell.

density accompanying the peritectic transformation leads to a volumetric contraction that shows up as wrinkling on the surface of the first layer of solid shell that forms against the copper mold. These observations were supported by both shell growth measurements and fiber-optic-based mold thermal mapping. Shell growth measurements were based on 3D light scanning of the shells which generated a high-resolution model of the shells that enabled very fast and accurate characterization. Shell deviation from absolute flatness and shell thickness variations are properties of the shells that were

used in the present study to characterize peritectic sensitivity. In addition, instantaneous mold thermal maps generated using imbedded optical fiber and Rayleigh scattering were found to correlate well with these shell growth measurements. The application of high-resolution mold thermal mapping to the peritectic solidification problem, which has not been reported previously in literature to be best of our knowledge, shows great promise in detecting peritectic sensitivity in more complex alloy systems.

ACKNOWLEDGMENTS

This work was sponsored by the Peaslee Steel Manufacturing Research Center (PSMRC) at the Missouri University of Science and Technology Rolla MO, USA. The authors here by express their gratitude to all industry members that are involved in this consortium for their financial and technical support.

CONFLICT OF INTEREST

The authors declare no conflict of interest.

OPEN ACCESS

This article is licensed under a Creative Commons Attribution 4.0 International License, which permits use, sharing, adaptation, distribution and reproduction in any medium or format, as long as you give appropriate credit to the original author(s) and the source, provide a link to the Creative Commons licence, and indicate if changes were made. The images or other third party material in this article are included in the article's Creative Commons licence, unless indicated otherwise in a credit line to the material. If material is not included in the article's Creative Commons licence and your intended use is not permitted by statutory regulation or exceeds the permitted use, you will need to obtain permission directly from the copyright holder. To view a copy of this licence, visit <http://creativecommons.org/licenses/by/4.0/>.

APPENDIX

See Figures A1, A2, A3 and Table AI.

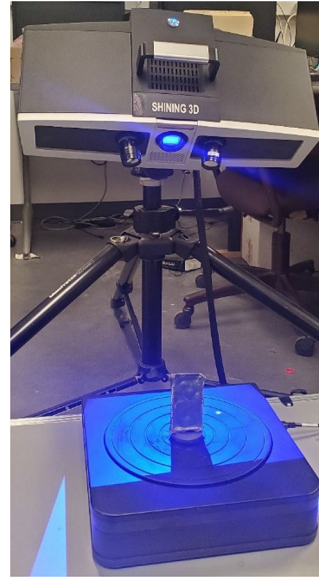


Fig. A1—Three-dimensional optical scanner used to produce accurate 3D models of the steel shell samples to a 40 μm resolution using a 360 deg turntable with shell firmly held on it.

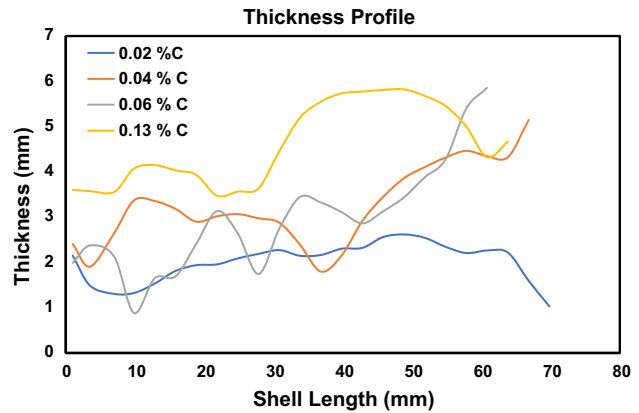


Fig. A2—Center-line shell thickness profile of four shells cast at 2 pct Mn with four levels of carbon—(0.02 pct C, 0.04 pct C, 0.06 pct C, 0.13 pct C). Rapid fluctuations in thickness are found in the peritectic grades—0.04 and 0.06 pct C.

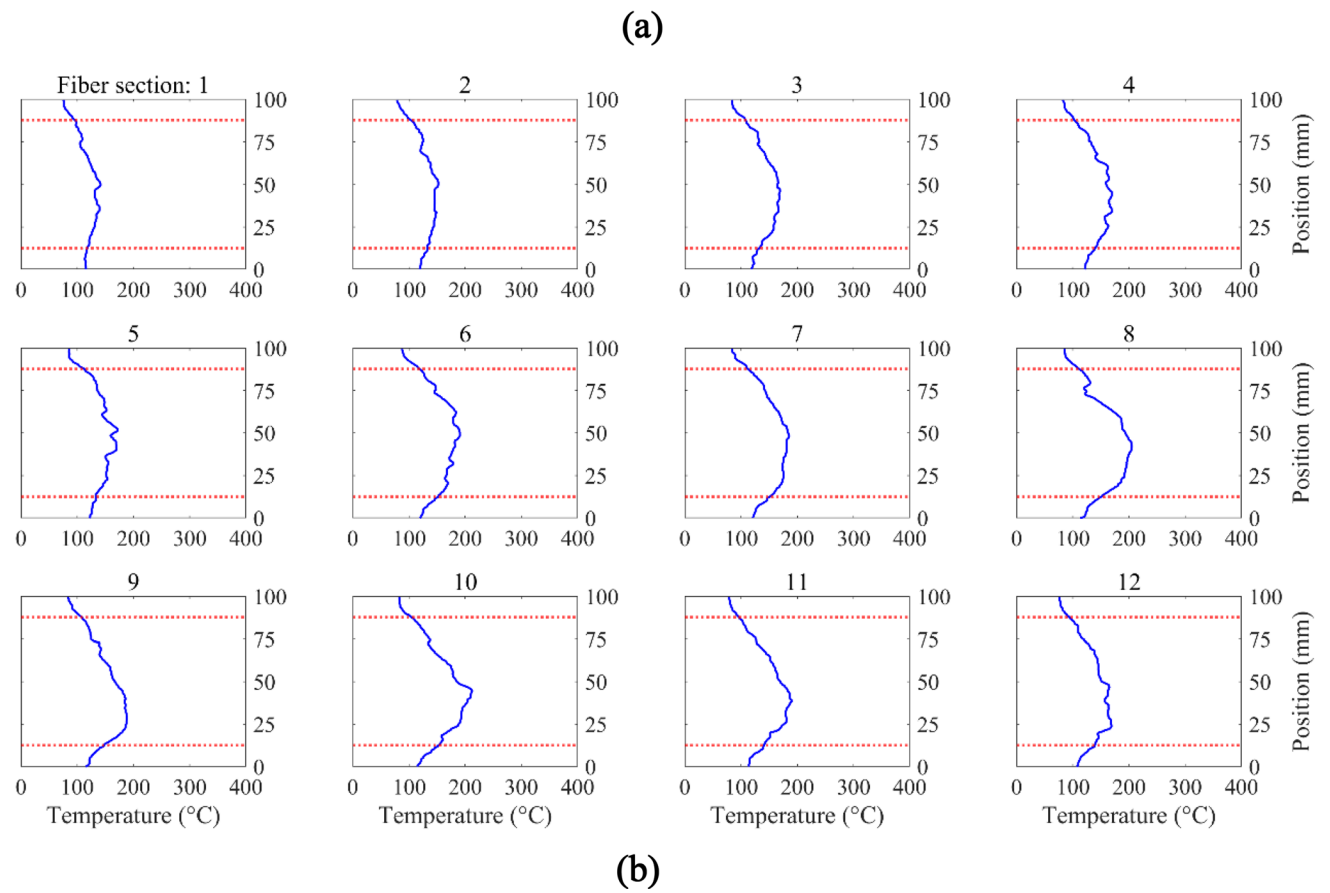
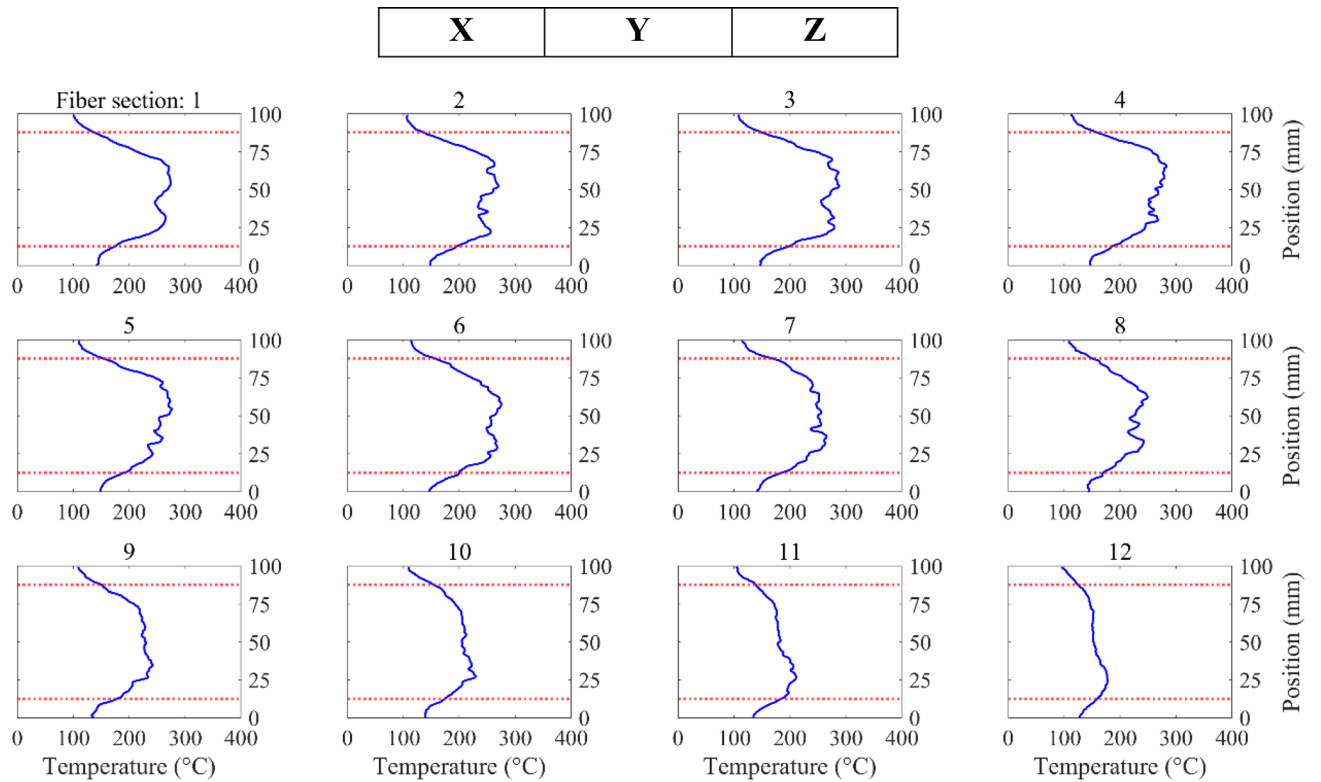


Fig. A3—Spatially distributed temperature profiles along twelve adjacent embedded optical fiber sections during two immersion tests. (a) The temperature profiles used to generate thermal map shown in Fig. 15(a). (b) The temperature profiles used to generate thermal map shown in Fig. 15(b).

Table AI. A Typical Output Data from the 3D Scanning of Steel Shells in an $N \times 3$ Matrix

X	Y	Z
10.52797	– 14.5273	39.27726
10.6223	– 14.5459	39.29982
10.60114	– 14.5426	39.16926
10.67354	– 14.5564	39.19333
10.74769	– 14.5639	39.20309
10.82435	– 14.5738	39.21995
10.56749	– 14.5324	39.03328
10.64732	– 14.55	39.05743
10.72335	– 14.5645	39.07522
10.79944	– 14.5732	39.09074
10.88038	– 14.5892	39.12105
10.95982	– 14.6055	39.14834
11.03836	– 14.6211	39.17291
11.11721	– 14.6404	39.20053
10.53762	– 14.5163	38.88919
10.62067	– 14.5386	38.91675
10.69741	– 14.5549	38.93901
10.77346	– 14.5688	38.95668
10.85402	– 14.5834	38.9859
10.93377	– 14.6005	39.01429
11.01383	– 14.6181	39.04316
11.09461	– 14.6383	39.07561
11.17181	– 14.6535	39.09768
11.2464	– 14.6631	39.10962
11.32146	– 14.6747	39.12416
10.49424	– 14.4896	38.72724
10.59223	– 14.5229	38.76748
10.67034	– 14.5405	38.79843
10.74673	– 14.558	38.81834
10.82694	– 14.5754	38.84796
10.90727	– 14.5956	38.87934
10.98922	– 14.6163	38.91415
11.07212	– 14.6355	38.95041
11.15014	– 14.6532	38.97588
11.22693	– 14.6666	38.99539

$N \sim 600,000$ points on the surface of the shell (truncated in the above table for space constraints). The measurements shown are those of the 2 pct Si shell with 0.06 pct C content.

REFERENCES

1. J.K. Brimacombe and K. Sorimachi: *Metall. Mater. Trans. B*, 1977, vol. 8B, pp. 489–505.

2. M. Wolf and W. Kurz: *Metall. Mater. Trans. B*, 1981, vol. 12B, pp. 85–93.

3. B.G. Thomas, M.S. Jenkins, and R.B. Mahapatra: *Ironmak. Steelmak.*, 2004, vol. 31, pp. 485–94.

4. ASM Handbook: in *Heat Treating*, vol. 4, ASM International, New York, 1991.

5. M.M. Wolf: in *Continuous Casting: Initial Solidification Strand Surface Quality of Peritectic Steels*, vol. 9, M.M. Wolf, ed., Iron and Steel Society/AIME, Warrendale, PA, 1997, pp. 61–65.

6. A. Grill and J. Brimacombe: *Ironmak. Steelmak.*, 1976, vol. 3, pp. 76–9.

7. S.N. Singh and K.E. Blazek: *JOM*, 1974, vol. 26, pp. 17–27.

8. T. Saeki, S. Oguchi, S. Mizoguchi, T. Yamamoto, H. Misumi, and S. Tuneoka: *Tetsu-to-Hagane*, 1982, vol. 68, pp. 1773–781.

9. J. Xu, S. He, X. Jiang, T. Wu, and Q. Wang: *ISIJ Int.*, 2013, vol. 53, pp. 1812–817.

10. R. Kuziak, R. Kawalla, and S. Waengler: *Arch. Civ. Mech. Eng.*, 2008, vol. 8, pp. 103–17.

11. H. Zhang and W. Wang: *Metall Mater Trans B*, 2017, vol. 48B, pp. 779–93. <https://doi.org/10.1007/s11663-016-0901-9>.

12. S.C. Zhang, Y.F. Geng, H.B. Li, et al.: *Metall Mater Trans B*, 2022, vol. 53B, pp. 4006–018. <https://doi.org/10.1007/s11663-022-02661-9>.

13. C. Lu, W. Wang, J. Zeng, et al.: *Metall Mater Trans B*, 2019, vol. 50B, pp. 77–85. <https://doi.org/10.1007/s11663-018-1449-7>.

14. B. De Cooman: *Curr. Opin. Solid State Mater. Sci.*, 2004, vol. 8, pp. 259–65.

15. P. Jacques: *Curr. Opin. Solid State Mater. Sci.*, 2004, vol. 8, pp. 259–65.

16. M. Roman, et al.: *IEEE Trans. Instrum. Meas.*, 2021, vol. 70, pp. 1–0.

17. I. Tamura, H. Sekine, and T. Tanaka: *Thermomechanical Processing of High Strength Low-Alloy Steels*, 1st ed. Butterworth-Heinemann, London, 1988, pp. 50–77.

18. K.H. Lee, M.C. Kim, B.S. Lee, and D.M. Wee: *J. Nucl. Mater.*, 2010, vol. 403, pp. 68–74.

19. M. El-Bealy and B.G. Thomas: *Metall Mater Trans B*, 1996, vol. 27B, pp. 689–93.

20. D. Balogun, M. Roman, R.E. Gerald-II, J. Huang, L. Bartlett, and R. O'Malley: *Steel Res. Int.*, 2021, <https://doi.org/10.1002/srin.202100455>.

21. H.W. Kerr, J. Cisse, and G. Bolling: *Acta Metall.*, 1974, vol. 22, pp. 677–86.

22. M. Roman, D. Balogun, R.E. Gerald II, J. Huang, L. Bartlett, and R. O'Malley: in *Proceedings of the AISTech 2020 (2020, Cleveland, OH)*, pp. 822–833, Association for Iron & Steel Technology (AIST), 2020.

23. H. Zhang and W. Wang: *Metall. Mater. Trans. B*, 2016, vol. 47B, pp. 920–31.

24. A. Badri, T. Natarajan, C. Snyder, K. Powers, F. Mannion, and A. Cramb: *Metall. Mater. Trans. B*, 2005, vol. 36B, pp. 355–71.

Publisher's Note Springer Nature remains neutral with regard to jurisdictional claims in published maps and institutional affiliations.